Physics and Chemistry of Minerals (2019) 46:827–837
https://doi.org/10.1007/s00269-019-01043-z

ORIGINAL PAPER

Experimental and calculated Raman spectra in Ca–Zn pyroxenes and a comparison between $(Ca_xM^{2+}{}_{1-x})M^{2+}Si_2O_6$ pyroxenes (M^{2+} = Mg, Co, Zn, Fe^{2+})

Mario Tribaudino[1] · Claudia Stangarone[1,3] · Claudia Gori[1] · Luciana Mantovani[1] · Danilo Bersani[2] · Pier Paolo Lottici[2]

Received: 1 April 2019 / Accepted: 3 June 2019 / Published online: 13 June 2019

Abstract

The Raman spectra of the end member pyroxenes $CaZnSi_2O_6$ and $Zn_2Si_2O_6$ are calculated by quantum mechanical modeling and compared with the experimental ones measured in synthetic $(Ca_xZn_{1-x})ZnSi_2O_6$ pyroxenes with $x = 0$, 0.2, 0.3, 0.5, 0.7, 1. The calculated spectra correctly predict the intensity and peak positions of the spectra recorded on the end members. The model provides also useful hints for the mode assignment at the intermediate compositions. The experimental peak positions are compared in $(Ca_xM^{2+}{}_{1-x})M^{2+}Si_2O_6$ pyroxenes, with M^{2+} = Mg, Co, Zn, Fe^{2+}. These pyroxenes share a common charge and different mass and ionic radius; the relative contributions of the mass and ionic radius in the experimental spectrum are discussed in four of the most intense peaks. We found that the positions of the strongest peaks are related to the average bond distances of the polyhedra which most affect a given mode. Ca–Zn pyroxenes provide an exception, whereas the $CaZnSi_2O_6$ end member fits quite well in the bond-distance/peak positions relations found in other pyroxenes, and the same does not occur as Zn exchanges for Ca. Peak broadening occurs in Zn pyroxenes in intermediate compositions; it is related to the presence of polyhedral local configurations around Zn and Ca atoms in the M2 polyhedron. The broadening is higher in the ~ 1010 cm^{-1} peak (ν_{19}), which, among the strongest peaks, shows the highest difference in the Raman wavenumber between end members. The different behaviours of Zn pyroxenes with respect to Mg, Co, and Fe^{2+} ones are likely related to the partially covalent bonding in the M2 cavity shown by Zn pyroxenes.

Keywords Pyroxene · Raman spectroscopy · Zn · Peak position and crystal structure

Introduction

Natural pyroxenes are major phases in high-temperature volcanic and basic plutonic rocks. The composition of most natural pyroxenes falls within the "quadrilateral pyroxene field"; their simplified formula is (Ca, Mg, Fe)SiO_3, with maximum Ca = 0.5 apfu. The holotypic *C*2/*c* pyroxene diopside, $CaMgSi_2O_6$, is an example of the structure of pyroxenes. In diopside, Ca is hosted in the large eightfold coordinated M2 site, Mg in the more regular octahedral M1 site, and Si in a tetrahedrally coordinated position (Fig. 1). Cation substitution may occur to various extents in M1 and M2 sites, but larger cations such as Ca and Na can enter only the M2 site. The substitution of a smaller cation for a larger one in the M2 site of diopside can occur up to a limited extent. A miscibility gap is present between Ca-rich and Ca-poor, natural pyroxenes, so that two different pyroxene phases coexist in natural basic and ultrabasic rocks. An

Electronic supplementary material The online version of this article (https://doi.org/10.1007/s00269-019-01043-z) contains supplementary material, which is available to authorized users.

✉ Mario Tribaudino
mario.tribaudino@unipr.it

[1] Department of Chemistry, Life Sciences and Environmental Sustainability, University of Parma, Parco Area delle Scienze 157/A, 43124 Parma, Italy

[2] Department of Mathematical, Physical and Computer Sciences, University of Parma, Parco Area delle Scienze 7/A, 43124 Parma, Italy

[3] Present Address: German Aerospace Center (DLR), Rutherfordstraße 2, 12489 Berlin, Germany

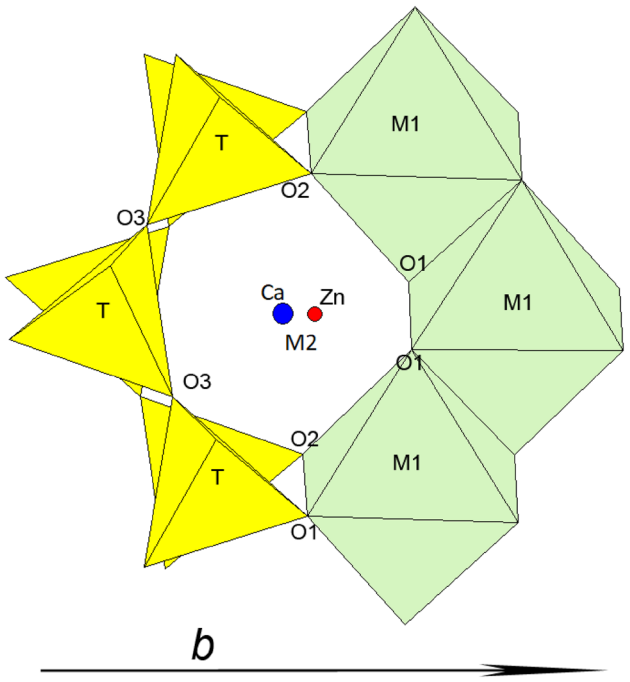

Fig. 1 Structure of Ca–Zn pyroxenes; view along [100]. The split subsites for Zn and Ca in the M2 cavity are shown. In Ca–Cn pyroxenes, M1 is filled by Zn and T by Si

asymmetric miscibility gap results, with larger solubility, in the Ca-richer side, i.e., when a larger cation is exchanged by a smaller one. The miscibility gap increases when the difference in cation radius is higher: when Mg (ionic radius 0.72 Å, Shannon 1976) exchanges for Ca, the pyroxene solubility is lower than when Fe (ionic radius 0.78 Å) enters for Ca (Mantovani et al. 2014). The miscibility gap is accompanied by a phase transition from Ca-richer $C2/c$ to $P2_1/c$ Ca-poorer pyroxenes.

However, the rather flexible structure of pyroxenes is able to host many other elements. For example, di-valent transition elements such as Zn and Co can enter the M2 site, and exchange with the larger Ca cation. In Ca–Co pyroxenes, studied along the $CaCoSi_2O_6$–$Co_2Si_2O_6$ series, a miscibility gap is present, such as in Ca–Mg ($CaMgSi_2O_6$–$Mg_2Si_2O_6$) and Ca–Fe pyroxenes ($CaFeSi_2O_6$–$Fe_2Si_2O_6$) (Mantovani et al. 2014). As expected, the solubility of Co in pyroxenes is intermediate between that of Mg and Fe in Ca–Mg and Ca–Fe pyroxenes, being the ionic radius of Co^{2+} (0.74 Å) intermediate between that of Mg and Fe. Moreover, the $C2/c$–$P2_1/c$ phase transition occurs also in Co pyroxenes, at 0.40 Ca apfu, which is intermediate between the composition at the transition of Ca–Mg and Ca–Fe pyroxenes (0.15 and 0.60 Ca apfu, respectively).

Ca–Zn pyroxenes along the $CaZnSi_2O_6$–$Zn_2Si_2O_6$ series show a different behavior, even if the ionic radius of Zn (0.745 Å, Shannon 1976) is very similar to that of Co. Zn can exchange for Ca to any extent, giving a complete solid solution: Ca–Zn pyroxenes display a $C2/c$ symmetry for any composition. It has been suggested that this depends on the peculiar distorted fourfold coordination of Zn within the M2 site, which is different from the octahedral coordination of Mg, Fe, and Co into the same site (Gori et al. 2015). The fourfold coordination has been related to the covalent character of the Zn bond in the M2 site (Morimoto et al. 1975).

As the vibrational behavior is related to the local structure, an investigation of the Raman spectra of Zn pyroxenes may give a clue to interpret the local configurations related to the entrance of Zn in the crystal structure.

In this work, a Raman investigation on Ca–Zn pyroxenes is reported. The spectra of the end members $CaZnSi_2O_6$ and $Zn_2Si_2O_6$ were calculated by quantum mechanical modelling and compared with the experimental ones on a series of synthetic $CaZnSi_2O_6$–$Zn_2Si_2O_6$ pyroxenes. In diopside, enstatite, and jadeite pyroxenes, the quantum mechanical simulation was able to describe the complex atomic vibrations involving $C2/c$ and $Pbca$ pyroxene structures (Prencipe 2012; Prencipe et al. 2012; Stangarone et al. 2016). The results provide the basis for a correct mode assignment, to interpret the relations between crystal structure and Raman spectra.

The calculated and experimental spectra were then compared with those of Ca–Mg and Ca–Co pyroxenes, belonging to the $CaMgSi_2O_6$–$Mg_2Si_2O_6$ and $CaCoSi_2O_6$–$Co_2Si_2O_6$ series. These pyroxenes show the same substitution of Ca for a smaller cation, with Co and Mg fixed in the M1 site, and exchanging for Ca in the M2 site.

The aim is to show how the M^{2+} cation for Ca substitution affects the Raman spectra and how the positions of the strongest peaks are related to the crystal structure.

Experimental

Sample characterization and Raman data collection

Raman spectra were measured on six synthetic clinopyroxenes with composition $Ca_xZn_{1-x}ZnSi_2O_6$ with $x = 0$, 0.2, 0.3, 0.5, 0.7, 1. The intermediate pyroxenes were synthesized at $P = 5$ GPa and $T = 1200$ °C, whereas the end members $CaZnSi_2O_6$ and $Zn_2Si_2O_6$ were synthesized at $P = 4$ GPa and $T = 1000$ °C. Synthesis details can be found in Gori et al. (2015).

The results of the chemical and structural characterizations using SEM–EDS microprobe analysis and single-crystal X-ray diffraction (SCXRD) on the above samples are reported in Gori et al. (2015). In Ca–Zn pyroxenes, SCXRD shows invariably $C2/c$ space group, whereas pyroxenes with Mg, Co, or Fe show $C2/c$ and $P2_1/c$ space group in Ca-richer and Ca-poorer samples, respectively (Ohashi et al. 1975;

Ohashi and Finger 1976; Tribaudino 2000; Tribaudino et al. 2002; Mantovani et al. 2014).

Raman measurements were carried out using a Horiba Jobin–Yvon LabRam with 1800 lines/mm grating and CCD detector (1024 × 256 pixels). The 632.8 nm line of an He–Ne laser was used for excitation and power on the sample was kept ≤ 1 mW. The wavenumber calibration was performed by the Raman peak of silicon. A 100 × objective with a 0.9 numerical aperture was used. Spatial resolution was about 1 µm, and the spectral resolution was about 2 cm^{-1} with an accuracy of ~ 0.5 cm^{-1}. Typical exposures were 60–240 s, repeated three times, depending upon the crystal size, the Raman scattering efficiency and the intensity (if any) of background fluorescence.

Raman analyses were made on loose grains without any sample preparation. Due to the small grain size, no attempt was made to take Raman spectra from oriented single crystals.

The peak positions were obtained from baseline-corrected spectra by a least-squares spectral curve-fitting routine using Labspec® software package. A pseudo-Voigt shape function was used for the peak profile analysis.

The spectra of $Ca_xZn_{1-x}ZnSi_2O_6$ are reported in Fig. 2; peak positions are reported in Table 1 and, for the peaks measured at least in four different samples, also in Fig. 3. As the end member $CaZnSi_2O_6$ ($x = 1$) showed strong fluorescence, only few strong peaks could be detected. In Fig. 2, only the calculated spectrum for the end member $CaZnSi_2O_6$ is shown.

The peak position ν_i, with i as label of a given peak, is reported in Table 1 and Fig. 3. In a loose sense, the ν_i labelling will be used to identify the peak position (wavenumber), the peak itself, and the corresponding vibrational mode from quantum mechanical calculations.

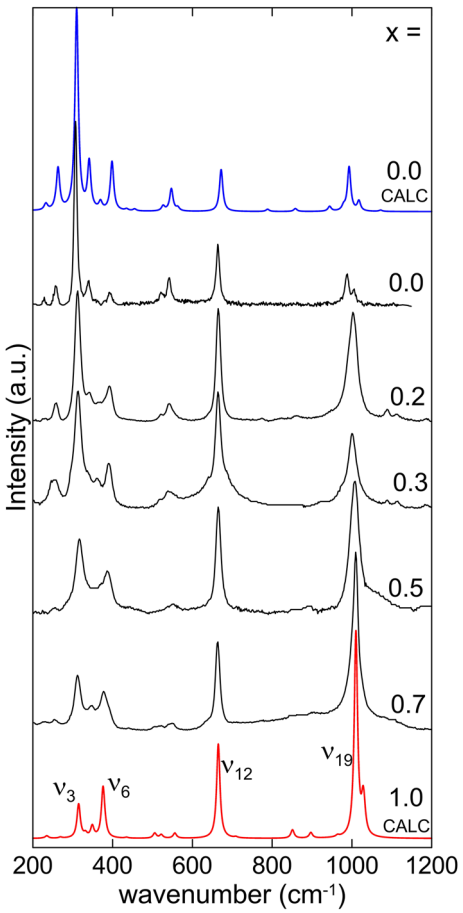

Fig. 2 Calculated and measured Raman spectra for Ca–Zn pyroxenes $(Ca_xZn_{1-x})ZnSi_2O_6$. The linewidth of the two calculated spectra was fixed to 10 cm^{-1}, so to be similar to the experimental one for the end members. Ca content on the right in apfu

Quantum mechanical calculations

Ab initio HF/DFT simulations were performed with CRYSTAL14 (Dovesi et al. 2014) employing the WC1LYP hybrid Hamiltonian which is most suitable for the calculation of the elastic and vibrational properties of crystals (Prencipe 2012, 2017; Aliatis et al. 2015; Stangarone et al. 2016, 2017). In this Hamiltonian, the Wu–Cohen DFT–GGA exchange contribution (Wu and Cohen 2006) is corrected by a percentage (16%) of the exact non-local Hartree–Fock exchange. The correlation is described by the LYP functional (Lee et al. 1988). The localized contracted atomic basis sets used were 86-311G(1d) (Pascale et al. 2004) for Si atoms, 8-411G(2d) (Valenzano et al. 2006) for O, 86-411d31G (Jaffe and Hess 1993) for Zn, and 86-511d21G (Valenzano et al. 2006) for Ca. The basis sets were taken from the repository at the address https://www.crystal.unito.it/basis-sets.php. In CRYSTAL, the level of accuracy in evaluating the Coulomb and Hartree–Fock exchange series is controlled by five parameters (Dovesi et al. 2014), specified by the TOLINTEG keyword: these parameters were set to 8, 8, 8, 8, and 18. The reciprocal space was sampled using a regular sublattice with a shrinking factor of 2, corresponding to 6 independent $\boldsymbol{k}$ vectors in the irreducible part of the Brillouin zone. The exchange–correlation DFT contributions to the Fock matrix were evaluated by numerical integration over the unit cell volume. Radial and angular points for the integration grid were generated through Gauss–Legendre radial quadrature and Lebedev two-dimensional angular point distributions. A pruned grid of 114,696 points in the unit cell for $CaZnSi_2O_6$, and 116,779 points for $Zn_2Si_2O_6$was generated. A measure of the high numerical accuracy reached is the evaluation of the total number of electrons in the unit cell by the numerical integration of the electron density over the cell volume: for $CaZnSi_2O_6$, we obtained 251.99992 electrons out of 252 and for $Zn_2Si_2O_6$ 271.99995, out of 272 at *static* equilibrium (i.e., 0 K and with no zero-point vibrational effects

Table 1 Calculated and experimental peak positions and slope m of the linear fit $y = mx \times 100 + y0$, with y the peak position, x the Ca content (apfu), y_0 the peak position at $x = 0$

$x \times 100$		0 calc	0	20	30	50	70	100	100 calc	Exp slope	Calc slope
ν_1	A_g	233	228.4		224.4		233.6		235		
ν_2	A_g	263	257.6	257.5	256.2	252.6	255.6		269	− 0.05(3)	0.06
ν_3	A_g	310	307.1	312.1	313.4	316.9	311.8	310.5	315	0.02(4)	0.05
ν_4	A_g	341	339.2	338.4	337.6	340.9	331.8		332	− 0.07(6)	− 0.09
ν_5	B_g	370		366.5	362.8	359.5	346.2	345.2	349	− 0.29(6)	− 0.21
ν_6	A_g	398	393.1	392.5	390.9	387.9	378.5	373.3	376	− 0.22(3)	− 0.22
ν_7	B_g						393.7		381		
ν_8	B_g	435		444.6	431.8	437.8	439.9		435	− 0.01(9)	0.00
ν_9	(A_g)						505.7		505		
ν_{10}	A_g	527	516.2	519.4	516.2	521.4	520.4		522	0.06(4)	− 0.05
ν_{11}	A_g	547	541.4	542.7	541.4	552.5	546.7		556	0.12(7)	0.09
ν_{12}	A_g	672	663.8	665.1	664.6	665.1	663.5	662.6	665	− 0.02(1)	− 0.07
ν_{13}	B_g						708.2		709		
ν_{14}	B_g	789		772.9			772.0				
ν_{15}	(A_g)								851		
ν_{16}	B_g	858		851.3		873.1	865.2				
ν_{17}	B_g						899.3		897		
ν_{18}	A_g	944	937.7	947.3	949.5	950.1			964	0.21(10)	0.20
ν_{19}	A_g	993	987.3	1000.5	1001.3	1006.4	1008.8	1011.0	1010	0.21(5)	0.17
ν_{20}	A_g	1018	1005.5						1028		0.10

The experimental slope is determined for unambiguously defined peaks throughout the series, with at least four values. The calculated slope is obtained by the difference between corresponding peaks in the DFT calculated end members divided by 100. The mode symmetry from the calculated spectra is reported. The symmetry of the modes is bracketed when present only in $CaZnSi_2O_6$

included). The crystal structures were optimized with CRYSTAL14 on the basis of analytical energy gradients with respect to fractional atomic coordinates and unit cell parameters (Doll et al. 2001). Default values were chosen for convergence of gradient components as well as nuclear displacements. For the optimized crystallographic structure, the calculation of all phonon modes at the Γ point was carried out at static equilibrium structure. Vibrational wavenumbers and normal modes were calculated within the limit of the harmonic approximation. The first derivatives of the energy with respect to the atomic positions are calculated analytically (Doll et al. 2001), whereas the second derivatives are numerically calculated by setting the nuclear displacements to 0.003 Å from the equilibrium positions. Relative Raman intensities were computed using a fully analytical approach (Maschio et al. 2013) implemented in the CRYSTAL14 program. It combines analytical gradients (Doll et al. 2001) with solutions of first-order and second-order coupled perturbed Hartree–Fock/Kohn–Sham equations for the linear and quadratic orbital responses to electric fields in the different Cartesian directions.

To assess the contribution of the reduced mass variation in going from $CaZnSi_2O_6$ to $Zn_2Si_2O_6$, the peak positions were also calculated from the structure of $Zn_2Si_2O_6$, but with Ca exchanging for Zn, taking advantage of the ISOTOPES subroutine in CRYSTAL14. As discussed by Stangarone et al. (2016), this procedure enables to separate the contributions due to the changing mass of the vibrating atoms, with those from the interatomic force constants.

In Tables 1, and in Figs. 2 and 3, the computed spectra and peak positions for $CaZnSi_2O_6$ and $Zn_2Si_2O_6$ are reported and compared with the experimental ones in $Ca_xZn_{1-x}ZnSi_2O_6$. In Table 2, the computed intensities, graphically shown in Fig. 2, are reported, as well as the frequency shift from isotopes substitution of Ca for Zn in the M2 site of the $Zn_2Si_2O_6$ structure. Numerical values of the intensity of the calculated peaks, at different orientations, are reported as supplementary materials S1 and S2 for $CaZnSi_2O_6$ and $Zn_2Si_2O_6$, respectively.

Results

Raman spectra of Ca–Zn pyroxenes

Factor-group analysis at $\Gamma = 0$ shows that $C2/c$ and $P2_1/c$ pyroxenes have 30 ($14A_g + 16B_g$) (Rutstein and White 1971) and 60 ($30A_g + 30B_g$) Raman active modes, respectively (Wang et al. 2001; Prencipe et al. 2012). Out of the 30 predicted modes, 19 were observed in the $C2/c$ structure of Ca–Zn pyroxenes. They were identified through the $Ca_xZn_{1-x}ZnSi_2O_6$ series taking advantage of the peak

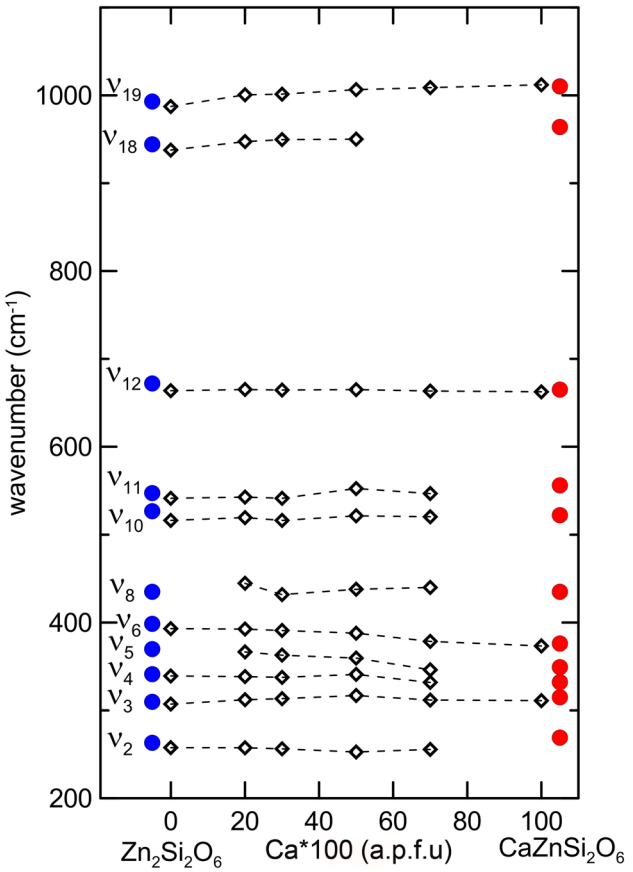

Fig. 3 Peak position vs composition in Ca–Zn pyroxenes (Ca_xZn_{1-x})$ZnSi_2O_6$ for the measured Raman peaks. The x marks the Ca content in atoms per formula unit. Red dots: calculated $CaZnSi_2O_6$; blue dots: calculated $Zn_2Si_2O_6$; diamonds: experimental Ca–Zn pyroxenes. The calculated peak positions of $CaZnSi_2O_6$ and $Zn_2Si_2O_6$, respectively, at 100 and 0 × coordinate are off shifted for clarity

positions and intensities from the calculated spectra. However, only a few strong peaks could be followed through the entire series (Table 1, Figs. 2 and 3).

Some modes, present in the calculated $CaZnSi_2O_6$ pyroxene, do not have corresponding features in $Zn_2Si_2O_6$: they are the A_g modes ν_9 and ν_{15} and the B_g modes ν_7 and ν_{14}. The peak at ~ 772 cm^{-1} found in $(Ca_{0.7}Zn_{0.3})ZnSi_2O_6$ and $(Ca_{0.2}Zn_{0.8})ZnSi_2O_6$ was ascribed to the ν_{14} B_g mode, which is present in calculated $Zn_2Si_2O_6$, but not in calculated $CaZnSi_2O_6$. The peak $A_g\nu_{15}$ is found only in calculated $CaZnSi_2O_6$, and has no experimental counterpart. The peak ν_{16} which could be related by the similar position was calculated as a B_g mode in $Zn_2Si_2O_6$ pyroxene.

Like in many $C2/c$ pyroxenes (Huang et al. 2000; Wang et al. 2001; Tribaudino et al. 2012; Mantovani et al. 2015), in Ca–Zn pyroxenes, the spectrum between 200 and 400 cm^{-1} shows a series of strong peaks, which were ascribed to M2- and M1–O bending and stretching vibrations (Prencipe et al. 2012; Stangarone et al. 2016). Among them, in $CaZnSi_2O_6$, there is a pair of strong peaks ν_3 and ν_6, with two other partially overlapping peaks in between, and a fainter one at 250 cm^{-1} (ν_2). At compositions $x < 0.5$, the peak ν_3 becomes most prominent and ν_2 gains intensity.

Between 400 and 800 cm^{-1}, we have few peaks related to the bending of the tetrahedral chains, with some contribution from the stretching in the M2 and M1 polyhedra (Prencipe et al. 2012): among these, the most intense is the peak at ~ 660 cm^{-1} (ν_{12}). This peak is single in $C2/c$ pyroxenes, but it splits in two peaks, as a consequence of the loss of equivalence of tetrahedral chains in the $P2_1/c$ structure (Ross and Reynard 1999; Tribaudino et al. 2012; Mantovani et al. 2015). Quantum mechanical simulation showed that the peak may be ascribed to a bending of the tetrahedral chain, and the different bendings of the two non-equivalent chains in $P2_1/c$ give a rationale for the two Raman peaks (Stangarone et al. 2016). In this range, we find the fainter peak ν_{11}, which gains intensity as x decreases, i.e., increasing Zn content.

At wavenumbers higher than 800 cm^{-1}, we observe peaks principally related to tetrahedral stretching. The most intense is the peak ν_{19}, which was related to the stretching of the two shorter tetrahedral bonds Si–O1 and Si–O2 atoms (Prencipe et al. 2012). In the calculated spectrum of $CaZnSi_2O_6$, the peak ν_{19} has a side peak at 1028 cm^{-1} (ν_{20}), which is present only in the calculated end members and in the $Zn_2Si_2O_6$ experimental spectrum. At intermediate compositions, it is likely overlapped with the broad ν_{19} peak.

Discussion

Comparison between Ca–Mg, Ca–Co, and Ca–Zn pyroxenes

In $CaZnSi_2O_6$ calculated Raman spectrum and in the $(Ca_{0.7}Zn_{0.3})ZnSi_2O_6$ experimental spectrum, the strongest peaks are ν_3, ν_6, ν_{12}, and ν_{19}: they have rather close intensity in the calculated $CaZnSi_2O_6$ (Fig. 2). As they are most intense also in $CaMgSi_2O_6$ and $CaCoSi_2O_6$ pyroxenes, these peaks can be linked to the corresponding peaks in synthetic $CaMgSi_2O_6$–$Mg_2Si_2O_6$ and $CaCoSi_2O_6$–$Co_2Si_2O_6$ pyroxenes.

The wavenumber of ν_3 shows a very small increase with increasing Ca (~ 5 cm^{-1}) in Ca–Zn pyroxenes (Fig. 4). Between $CaZnSi_2O_6$ and $(Ca_{0.3}Zn_{0.7})ZnSi_2O_6$, we observe a trend very similar to that found in Ca–Co pyroxenes between. For higher Zn content, Ca–Zn pyroxenes show higher wavenumber than Ca–Co ones. This difference, albeit small, is likely related to the $P2_1/c$–$C2/c$ phase transition in Co pyroxenes. In Co pyroxenes, a sharp turnover is present at 0.4 Ca apfu. The composition marks the transition between $C2/c$ and $P2_1/c$ space groups, whereas the same

Table 2 Calculated frequencies (cm^{-1}) and relative intensities of the modes in $CaZnSi_2O_6$ and $Zn_2Si_2O_6$

$CaZnSi_2O_6$			$Zn_2Si_2O_6$			Isotopes	
	Freq	Int		Freq	Int	$\Delta\nu$	
B_g	111	0.1	B_g	102	15.4	− 1.3	
A_g	130	0.7	A_g	109	30.7	− 2.1	
B_g	142	0.4	B_g	123	2	− 12.9	
B_g	155	0.2	A_g	128	2.7	− 10.7	
A_g	162	0.4	A_g	142	17.8	− 6.7	
A_g	171	0.5	B_g	142	1.0	− 9.7	
B_g	185	0.1	B_g	151	2.0	− 6.6	
B_g	225	0.1	B_g	231	1.3	− 4.2	
A_g	235	1.2	A_g	233	2.0	− 5.7	ν_1
A_g	269	0.5	B_g	257	0.9	− 14.9	
B_g	285	0.0	A_g	263	20.6	− 15.4	ν_2
B_g	314	2.7	B_g	305	1.8	0.8	
A_g	315	13.9	A_g	310	100	− 1.5	ν_3
A_g	332	1.8	A_g	341	23.7	0.1	ν_4
B_g	349	5.5	B_g	370	3.8	− 3.4	ν_5
A_g	376	24.2	A_g	398	24.5	0.4	ν_6
B_g	381	1.9	B_g	435	0.8	− 8.7	ν_8
B_g	435	0.4	B_g	455	0.9	− 3.6	
A_g	505	1.0	A_g	527	2.5	− 1.3	ν_{10}
B_g	506	1.5	B_g	537	0.1	− 5.7	
A_g	522	1.7	A_g	547	11.2	− 0.9	ν_{11}
Bg	556	2.5	B_g	563	1.6	− 21.1	
A_g	665	46.0	A_g	672	20.9	0.0	ν_{12}
B_g	709	0.5	B_g	789	1.1	0.8	ν_{14}
A_g	851	4.1	B_g	858	1.4	0.2	ν_{16}
B_g	897	2.7	A_g	944	2.4	1.5	ν_{18}
B_g	964	0.8	B_g	979	2.1	1.4	
A_g	1010	100	A_g	993	22.1	2.1	ν_{19}
A_g	1028	14.6	A_g	1018	4.9	1.9	ν_{20}
B_g	1031	5.5	B_g	1072	0.6	2.0	

In the column Isotopes the difference in frequency (cm^{-1}) between the $Zn_2Si_2O_6$ calculated and a fictive one with the same structure, but Ca replacing Zn is reported. Frequencies used in the structure vs composition are shown in bold

transition is not present in Ca–Zn pyroxenes (Mantovani et al. 2015). In Ca–Mg pyroxenes instead, the same peak increases by 17 cm^{-1}, as Mg enters for Ca (Fig. 4).

As for the ν_6 peak, Ca–Zn and Ca–Co pyroxenes follow almost the same trend, without an apparent effect of the phase transition. Instead, in Mg pyroxenes, the corresponding peak shows a marked turnover at the transition (Tribaudino et al. 2012).

The position of the ν_{12} peak changes little throughout the Ca–Zn series. Its position is very close to that of the corresponding peak in Ca-richer *C*2/*c* and to one of the two split peaks in $P2_1/c$ Ca-poorer Ca–Mg and Ca–Co pyroxenes.

Finally, the peak ν_{19} decreases with Ca in a way similar in Ca–Co and Ca–Zn pyroxenes, whereas in Ca–Mg pyroxenes, it does not show significant changes with composition. In pure $CaMgSi_2O_6$, $CaZnSi_2O_6$ and $CaCoSi_2O_6$, the wavenumber of the ν_{19} peak is similar, whereas with lower Ca content, the same peak shows a marked difference in Ca–Mg pyroxenes, compared with Ca–Co and Ca–Zn pyroxenes.

Peak positions and crystal structure

Table 1 shows the slope of wavenumber vs Ca content for the different Raman peaks in Ca–Zn pyroxenes (Ca_xZn_{1-x}) $ZnSi_2O_6$. The slope was calculated both from the experimental and the calculated spectra. In the calculated spectra, it is given by the difference in the peak positions between the computed spectra of $CaZnSi_2O_6$ and $Zn_2Si_2O_6$, and in the experimental ones by a linear fit of the peak position

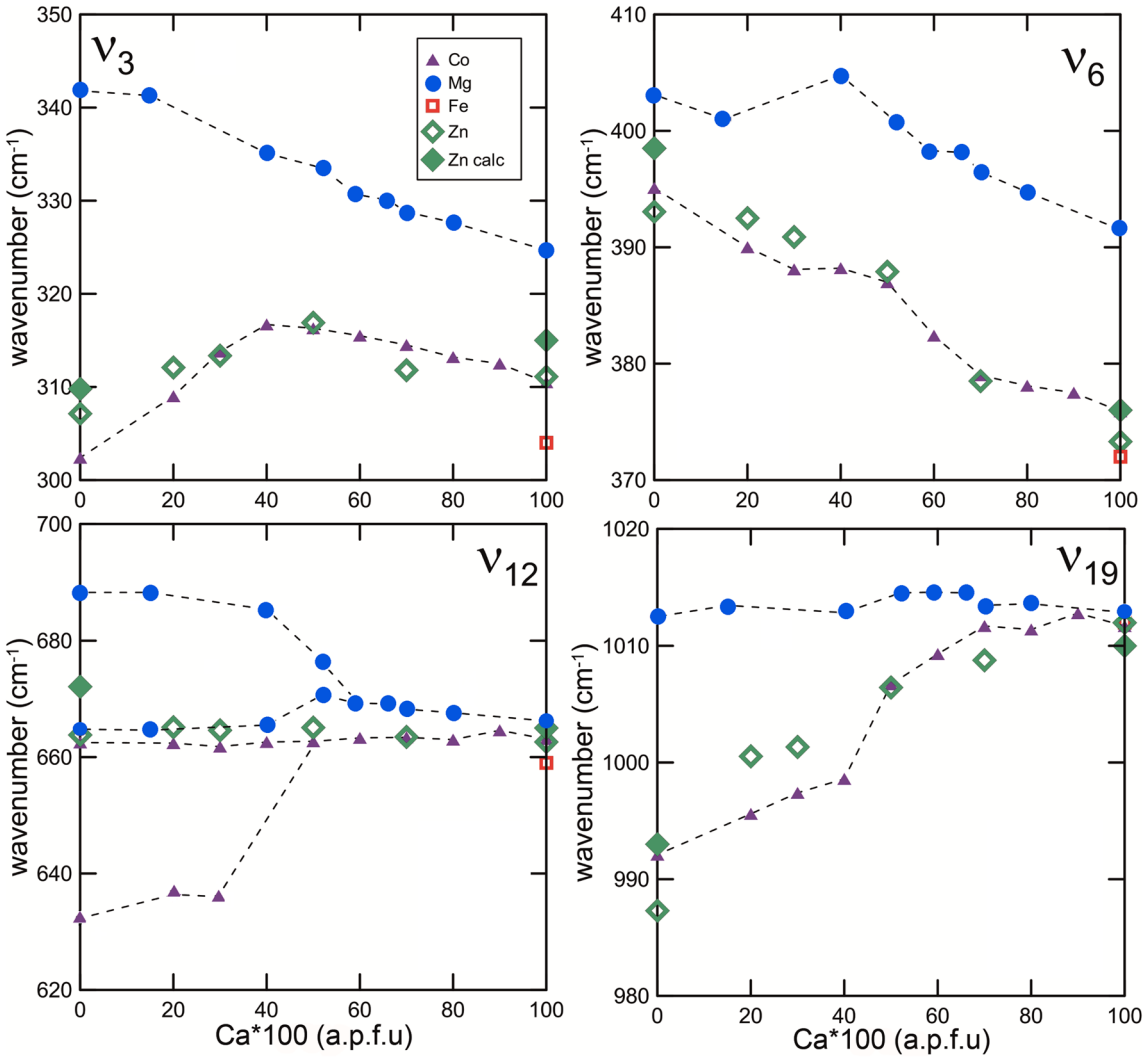

Fig. 4 Peak position of the main peaks in Raman spectra of Ca–Zn, Ca–Co, and Ca–Mg pyroxenes. Data for the hedenbergite ($CaFeSi_2O_6$ Ohashi et al. 1975) have been shown for comparison

(slope $= \partial\nu/\partial x$, ν mode frequency and $x =$ Ca expressed as apfu $\times$ 100).

A slight deviation from a linear behaviour was found only for the ν_3 peak, which shows an increase up to $(Ca_{0.5}Zn_{0.5})ZnSi_2O_6$ and a slight decrease at higher Ca content. The calculated and experimental slopes of the stronger peaks agree within error, with the exception of the peak ν_{12}, whose slope is lower than in the calculated spectrum (Table 1). The four peaks showing the highest absolute slopes in calculated spectra do the same in the experimental ones (Table 1).

In the 300–400 cm^{-1} range, we find a very small positive slope for the peak ν_3 and a negative one for the other three peaks: ν_5 and ν_6 show the most negative slope among the measured spectra. On the other side, ν_{18} and ν_{19} peaks, with the highest wavenumbers, show the highest positive slope. For the other peaks, the slope is lower, and hardly significant (Table 1).

The observed shifts in composition are likely due to structural changes which reflect upon the force constants of the various "bonds" and, hence, on the frequencies themselves. Moreover, also the changing mass has to be considered, as frequencies are given by the square roots of the eigenvalues of the Hessian matrix divided by the reduced mass associated to each mode. Such reduced mass is generally higher in ZnZn than in CaZn, so as a rule of thumb, frequencies should decrease in going from CaZn to ZnZn even if structural features and bond forces were hypothetically the same in the two end members. However, not all of the modes would be affected by such mass change: the reduced mass depends upon details of the normal modes (eigenvectors of the Hessian matrix), or by the symmetry of the mode and the site symmetry of the cation. As shown by ISOPTOPES calculation, for instance, the

higher frequency modes, most related by T–O stretching, are almost unaffected by the changing mass in the M2 site.

In the four most prominent and better measured peaks (ν_3, ν_6, ν_{12}, and ν_{19}), the mass contribution to the frequency shift is trivial (Table 2), so that we may explain their frequency shift results by an analysis of the most prominent structural changes due to Ca–Zn exchange (Gori et al. 2015) and by the quantum mechanical mode assignments to specific vibrational patterns (Prencipe et al. 2012; Stangarone et al. 2016), rather than by mass variation.

As shown by Prencipe et al. (2012), the modes in the 300–400 cm^{-1} range are ascribed to tetrahedral bending, with a strong involvement of the bonding of oxygen with the M2 cation, whereas the higher wavenumber peaks are related to intra-tetrahedral Si–O stretching, with no contribution from the other cations. Namely, the highest wavenumber modes are most related to the stretching of the shorter Si–O1 and Si–O2 bonds. Structural investigation shows that an increased substitution of the larger Ca for Zn increases the M2–O bond distances reducing the M2–O bond strength, most in shorter M2–O1 and M2–O2 bonds (Gori et al. 2015). As a general rule, we expect, therefore, that the modes which are affected by M2–O bonding, like those between 300 and 400 cm^{-1}, decrease their wavenumber with increasing Ca content. This is actually observed in three out of four of the modes in that range. To note, in Ca–Zn pyroxenes, the effect on the wavenumber of the lower mass of Ca is more than compensated by the increased M2–O bond distances.

A side effect of the increased M2–O distances with Ca substitution is, as the O1 and O2 oxygen are bonded also to tetrahedral Si, a decreased Si–O1, and Si–O2 distance. In this case, we may predict that the wavenumber of the modes related to Si–O1 and O2 stretching increases with Ca. This actually occurs for ν_{19} (Fig. 4).

On the other hand, in peaks such as ν_{12}, related to the M1–O average bond distances (Lambruschi et al. 2015), we expect little difference in the $Ca_xZn_{1-x}ZnSi_2O_6$ series, as the M1 site is occupied by Zn in the whole series.

The above picture is clearly oversimplified and must be checked against the actual structural findings, and comparing the results for Ca–Zn with those for Ca–Mg, Ca–Co, and Ca–Fe pyroxenes (Ohashi et al. 1975; Tribaudino et al. 1989, 2018; Prencipe et al. 2000; Mantovani et al. 2014; Gori et al. 2015). In Fig. 5, the wavenumbers of the four most prominent Raman peaks are shown as a function of bond distances. Only *C*2/*c* pyroxenes were taken into account, to get rid of the influence of the *C*2/*c*–*P*2_1/*c* transition on the crystal structure.

As expected, for ν_3 and ν_6 peaks, we find in Ca–Mg, Ca–Co, and Ca–Zn series, a decreased wavenumber as Ca exchanges for a smaller cation, increasing the M2–O bond distances. The lower mass of Mg with respect to Co and Zn accounts for the higher wavenumber of Ca–Mg pyroxenes. The exception is found in Zn richer compositions for the ν_3 peak, which show an opposite trend: as bond distances increase, also the wavenumber increases.

As concerns the ν_{12} peak, we see that Ca–Co, Ca–Mg, and Ca–Fe pyroxenes, for any exchange of Ca with a smaller cation, show a linear trend between wavenumber and bond distances, as previously found in a series of silicates and germanates with pyroxene structure and Ca in the M2 site (Lambruschi et al. 2015). On the contrary, Ca–Zn pyroxenes deviate significantly: M1–O distances increase with Zn content, whereas the wavenumber of the ν_{12} peak is almost constant (Fig. 5).

Quantum mechanical modelling related the peak at ν_{19} position to the stretching of the shorter tetrahedral bonds, i.e., the T–O1 and T–O2, the average of which is defined as average tetrahedral non bridging bond distance (T_{nbrg}). We could then expect some relation between T_{nbrg} and the position of the ν_{19} peak. In fact, Ca–Co pyroxenes follow an almost linear relation between wavenumber and T_{nbrg}, whereas in Ca–Mg pyroxenes, the position of the ν_{19} peak seems unaffected by the small changes in bond distances (Fig. 5). In Ca–Zn pyroxenes, between $CaZnSi_2O_6$ and $(Ca_{0.5}Zn_{0.5})ZnSi_2O_6$, the T_{nbrg} bond distances increase, but the ν_{19} peak position does not, whereas between $(Ca_{0.5}Zn_{0.5})ZnSi_2O_6$ and $Zn_2Si_2O_6$, the ν_{19} peak position decreases, although bond distances change only little.

It is interesting to note that the peak position in the Ca-end members is very similar in Zn, Mg, Co, and Fe pyroxenes.

It appears that, although the $CaZnSi_2O_6$ end member falls in a wavenumber—bond-distance trend similar to that of other pyroxenes, as Zn enters the M2 site, the Ca–Zn pyroxenes do not follow the simple wavenumber–structure relations which hold in Ca–Mg and Ca–Zn pyroxenes. It is then suggested that this occurs, as, with ongoing substitution of Zn for Ca, the M2–O bonding changes from ionic to partially covalent character (Gori et al. 2015).

Raman spectra and local structural configurations

Figure 6 shows the linewidth, defined as full-width at half-maximum (FWHM), vs composition of the two intense peaks ν_{12} and ν_{19}. The linewidths in the end members are similar, near to 9 cm^{-1}; they increase at the intermediate compositions, more for the ν_{19} peak. Local structural configurations were invoked to account for the increased linewidth in intermediate compositions of Ca–Co and Ca–Mg pyroxenes (Tribaudino et al. 1989, 2018; Mantovani et al. 2013). In the M2 polyhedron, we have different local structural environments when the polyhedron is centred on Ca or on a smaller cation. As a result, locally, different M2–O bond distances are present, which induce a non-periodic strain in the structure. The relevant strained texture was observed

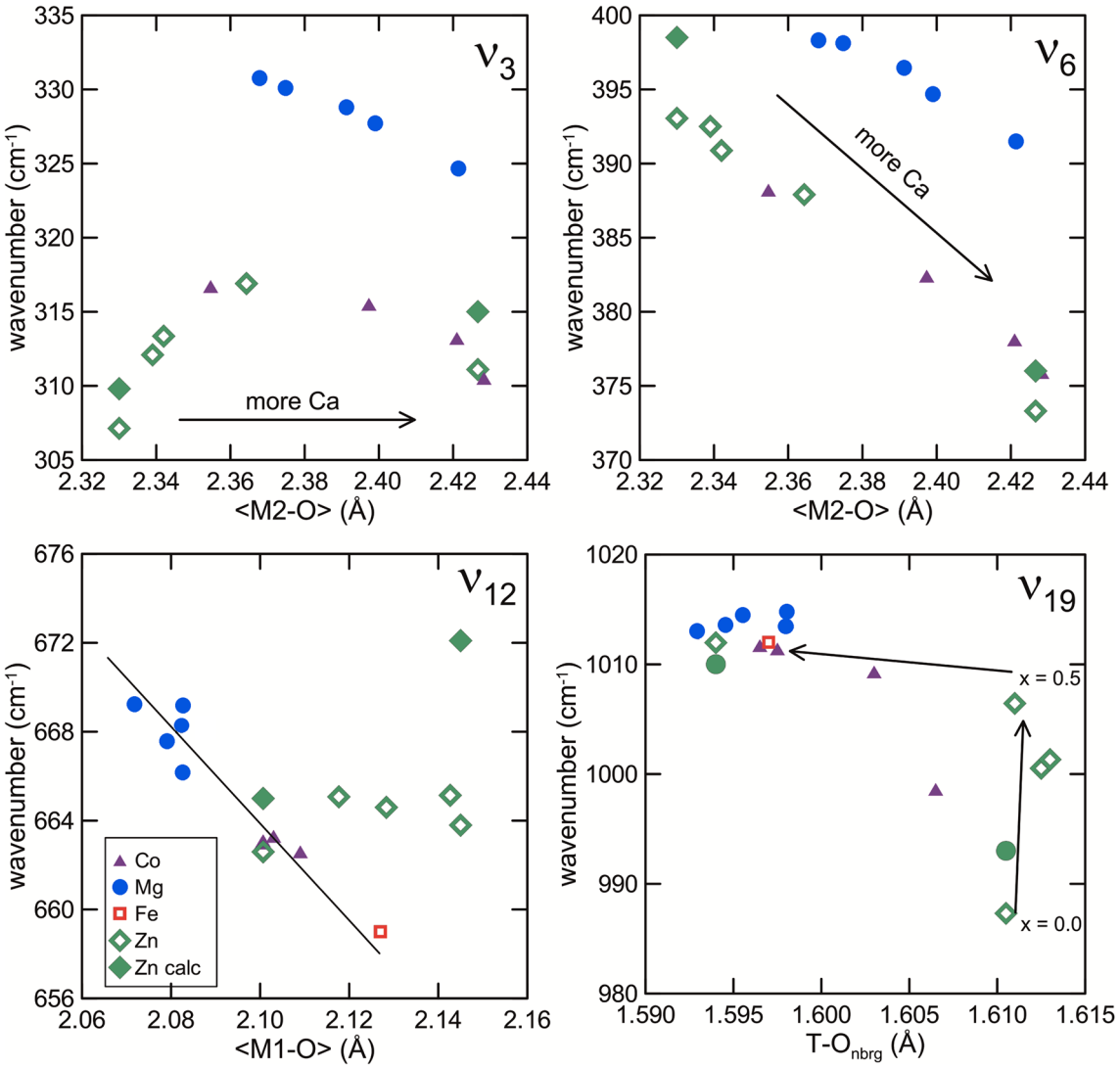

Fig. 5 Wavenumber of ν_3, ν_6, ν_{12}, and ν_{19} modes vs bond distance in Ca–Mg, Ca–Co, Ca–Zn, and $CaFeSi_2O_6$ pyroxenes. Arrows in ν_3, ν_6, and ν_{19} indicate the direction of increasing Ca content. The fit in the plot for peak ν_{12} is a best fit obtained from the peak positions of the $CaCoSi_2O_6$, $CaMgSi_2O_6$, $CaFeSi_2O_6$, and $CaZnSi_2O_6$ end members; only the Ca–Zn pyroxenes deviate from the fit, more as Zn increases

in Ca–Mg pyroxenes by transmission electron microscopy (Tribaudino 2000; Weinbruch et al. 2003).

The presence of local structural configurations in the M2 polyhedron affects the tetrahedral bond distances, mostly that between Si and the O2 oxygen (Tribaudino et al. 1989, 2018; Gori et al. 2015). On average, it was found that Si–O2 bond distances are longer when the O2 atom is linked with Ca, and shorter when it is linked by a smaller cation. We expect that this will occur also locally, so that different local configurations for tetrahedral bond distances exist. In a Raman spectrum, a disorder induced broadening is expected, and indeed found, in the peaks, whose modes are related to Si–O stretching, such as the peak ν_{19}.

In Fig. 7, the linewidth of the ν_{19} peak has been plotted in $(Ca_xM^{2+}{}_{1-x})M^{2+}Si_2O_6$ pyroxenes, with x between 1 and 0.5. The linewidth increases with the exchange of a smaller cation for Ca in all the series, but at a different rate. In Ca–Zn and Ca–Co pyroxenes, the same exchange of the smaller cation for Ca increases the linewidth more than in Ca–Mg pyroxenes. There is a relation with the difference in the position of the ν_{19} peak between the end members and the linewidth in the intermediate compositions: between $CaZnSi_2O_6$ and $Zn_2Si_2O_6$, and between $CaCoSi_2O_6$ and $Co_2Si_2O_6$, the difference is 23.7 and 19.6 cm^{-1}, respectively, whereas between $CaMgSi_2O_6$ and $Mg_2Si_2O_6$, it is just 4 cm^{-1}. This indicates that broader peaks are found at intermediate compositions when there is a higher difference between the peak positions of the end members, as it is observed in Ca–Zn and Ca–Co pyroxenes with respect to Ca–Mg ones.

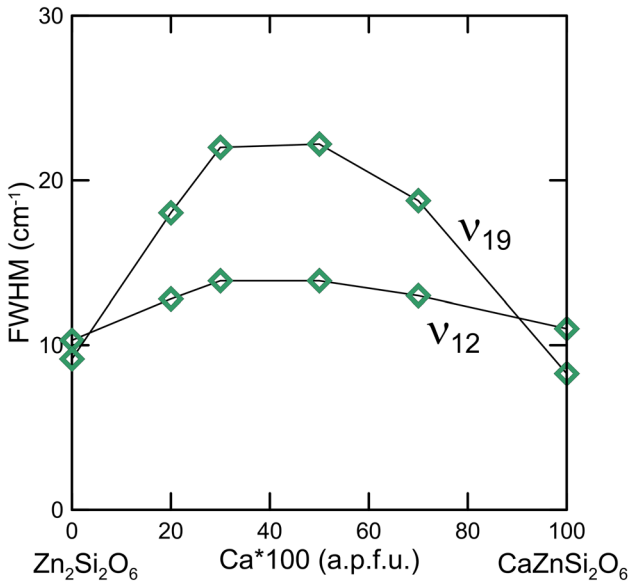

Fig. 6 FWHM vs composition for Ca–Zn pyroxenes $(Ca_xZn_{1-x})ZnSi_2O_6$ for ν_{12} and ν_{19} peaks

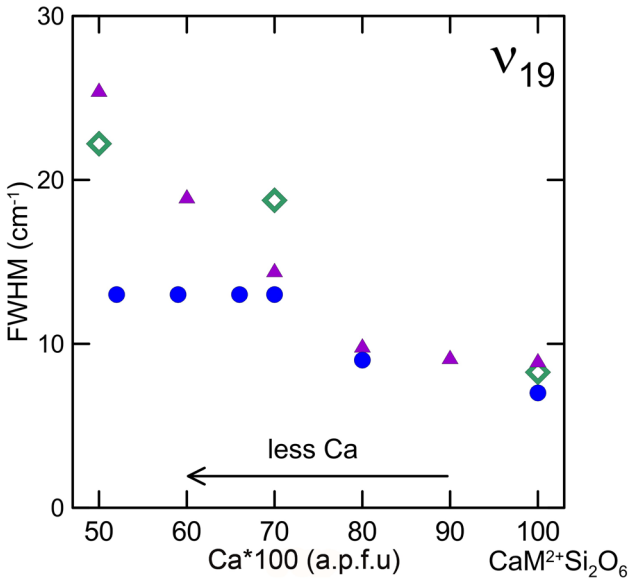

Fig. 7 FWHM of the ν_{19} peak in *C*2/*c* Ca–Co, Ca–Mg and Ca–Zn pyroxenes for *x* between 1 and 0.5. Symbols as in Fig. 5

The higher difference between the peak position of the end members in the ν_{19} vs ν_{12} peaks may also explain why the ν_{19} peak is broader for intermediate compositions: in Ca–Zn pyroxenes, the positions of the ν_{19} and ν_{12} peaks change between the end members by 23.7 and 1.2 and cm^{-1}, whereas the same peaks broaden by 13 and 4 cm^{-1}, respectively.

Conclusions

Quantum mechanical calculations for the end member structures provide a reference well suited to interpret the observed peak positions in the whole series of $(Ca_xZn_{1-x})ZnSi_2O_6$ pyroxenes. In $Zn_2Si_2O_6$, although with an overestimation between 3 and 12 cm^{-1} in peak position, the remarkable similarity with the measured spectrum provides the basis for peak assignment. In $CaZnSi_2O_6$, where a good quality spectrum could not be obtained, the calculations provide a suitable spectrum to replace the experimental one, highly affected by fluorescence. The slope of peak position vs composition is quite similar between experimental and calculated spectra.

The Raman wavenumber and FWHM change similarly in Ca–Co and Ca–Zn pyroxenes. Intermediate compositions show broader peaks, mostly in the ν_{19} peak related to intra-tetrahedral stretching.

On the other side, the Raman peak position changes with M2-, M1-, and T–O bond distances in a way significantly different in Ca–Zn pyroxenes with respect to Ca–Co and Ca–Mg ones. This may be related to the peculiar partially covalent bonding in the M2 cavity shown by Zn pyroxenes.

Acknowledgements Helpful and constructive revisions by two anonymous reviewers significantly improved this paper and are acknowledged. This work was supported by MIUR funding PRIN2010-2011 (2010EARRRZ_005).

References

Aliatis I, Lambruschi E, Mantovani L, Bersani D, Andò S, Gatta GD, Gentile P, Salvioli-Mariani E, Prencipe M, Tribaudino M, Lottici PP (2015) A comparison between ab initio calculated and measured Raman spectrum of triclinic albite ($NaAlSi_3O_8$). J Raman Spectrosc 46:501–508

Doll K, Saunders VR, Harrison NM (2001) Analytical Hartree–Fock gradients for periodic systems. Int J Quantum Chem 82:1–31

Dovesi R, Orlando R, Erba A et al (2014) CRYSTAL14: a program for the ab initio investigation of crystalline solids. Int J Quantum Chem 114:1287–1317

Gori C, Tribaudino M, Mantovani L, Delmonte D, Mezzadri F, Gilioli E, Calestani G (2015) Ca–Zn solid solutions in *C*2/*c* pyroxenes: synthesis, crystal structure and implications on Zn geochemistry. Am Mineral 100:2209–2218

Huang E, Chen CH, Huang T, Lin EH (2000) Xu Ji-An Raman spectroscopic characteristics of Mg–Fe–Ca pyroxenes. Am Mineral 85:473–479

Jaffe JE, Hess AC (1993) Hartree–Fock study of phase changes in ZnO at high pressure. Phys Rev B 48:7903–7909

Lambruschi E, Aliatis I, Mantovani L, Tribaudino M, Bersani D, Redhammer G, Lottici PP (2015) Raman spectroscopy of $CaM^{2+}Ge_2O_6$ (M^{2+} = Mg, Mn, Fe Co, Ni, Zn) clinopyroxenes. J Raman Spectrosc 46:586–590

Lee CT, Yang WT, Parr RG (1988) Development of the Colle-Salvetti correlation-energy formula into a functional of the electron-density. Phys Rev B 37:785–789

Mantovani L, Tribaudino M, Mezzadri F, Calestani G, Bromiley G (2013) The structure of (Ca, Co)$CoSi_2O_6$ pyroxenes and the Ca-M^{2+} substitution in (Ca,M^{2+})$M^{2+}Si_2O_6$ pyroxenes (M^{2+} = Co, Fe, Mg). Am Mineral 98:1241–1252

Mantovani L, Tribaudino M, Bertoni G, Salviati G, Bromiley G (2014) Solid solutions and phase transitions in (Ca, M^{2+})$M^{2+}Si_2O_6$ pyroxenes (M^{2+} = Co, Fe, Mg). Am Mineral 99:704–711

Mantovani L, Tribaudino M, Aliatis I, Lambruschi E, Bersani D, Lottici PP (2015) Raman spectroscopy of $CaCoSi_2O_6$–$Co_2Si_2O_6$ clinopyroxenes. Phys Chem Miner 42:179–189

Maschio L, Kirtman B, Salustro S, Zicovich-Wilson CM, Orlando R, Dovesi R (2013) Raman spectrum of pyrope garnet. A quantum mechanical simulation of frequencies, intensities, and isotope shifts. J Phys Chem A 117:11464–11471

Morimoto N, Nakajima Y, Syono Y, Akimoto S, Matsui Y (1975) Crystalstructure of pyroxene-type $ZnSiO_3$ and $ZnMgSi_2O_6$. Acta Cryst B31:1041–1049

Ohashi Y, Finger LW (1976) The effect of Ca substitution on the structure of clinoenstatite. Carnegie Inst Wash Year Book 75:743–746

Ohashi Y, Burnham CW, Finger LW (1975) The effect of Ca–Fe substitution on the clinopyroxene crystal structure. Am Mineral 60:423–434

Pascale F, Zicovich-Wilson CM, López Gejo F, Civalleri B, Orlando R, Dovesi R (2004) The calculation of the vibrational frequencies of crystalline compounds and its implementation in the CRYSTAL code. J Comput Chem 25:888–897

Prencipe M (2012) Simulation of vibrational spectra of crystals by ab initio calculations: An invaluable aid in the assignment and interpretation of the Raman signals. The case of jadeite ($NaAlSi_2O_6$). J Raman Spectrosc 43:1567–1569

Prencipe, M. (2018) Quantum mechanics in Earth sciences: a one-century-old story. Rend. Fis. Acc. Lincei, 1-21. Topical collection, Lincei Prize winners. https://doi.org/10.1007/s12210-018-0744-1

Prencipe M, Tribaudino M, Pavese A, Hoser A, Reehuis M (2000) Single-crystal neutron-diffraction investigation of diopside at 10 K. Can Mineral 38:183–189

Prencipe M, Mantovani L, Tribaudino M, Bersani D, Lottici PP (2012) The Raman spectrum of diopside: a comparison between ab initio calculated and experimentally measured frequencies. Eur J Mineral 24:457–464

Ross NL, Reynard B (1999) The effect of iron on the $P2_1/c$ to $C2/c$ transition in (Mg, Fe)SiO_3 clinopyroxenes. Eur J Mineral 11:585–589

Rutstein MS, White WB (1971) Vibrational spectra of high-calcium pyroxenes and pyroxenoids. Am Mineral 56:877–887

Shannon R (1976) Revised effective ionic radii and systematic studies of interatomic distances in halides and chalcogenides. Acta Cryst A32:751–767

Stangarone C, Tribaudino M, Prencipe M, Lottici PP (2016) Raman modes in *Pbca* enstatite ($Mg_2Si_2O_6$): an assignment by quantum mechanical calculation to interpret experimental results. J Raman Spectrosc 47:1247–1258

Stangarone C, Böttger U, Bersani D, Tribaudino M, Prencipe M (2017) Ab initio simulations and experimental Raman spectra of Mg_2SiO_4 forsterite to simulate Mars surface environmental conditions. J Raman Spectrosc 48:1528–1535

Tribaudino M (2000) A transmission electron microscope investigation on the $C2/c$ -$P2_1/c$ phase transition in clinopyroxenes along the diopside-enstatite ($CaMgSi_2O_6$-$Mg_2Si_2O_6$) join. Am Mineral 85:707–715

Tribaudino M, Benna P, Bruno E (1989) Average structure and M2 site configurations in $C2/c$ clinopyroxenes along the Di-En join. Contr Mineral Petrol 103:452–456

Tribaudino M, Nestola F, Cámara F, Domeneghetti MC (2002) The high temperature $P2_1/c$-$C2/c$ phase transition in Fe-free pyroxene ($Ca_{0.15}Mg_{1.85}Si_2O_6$): structural and thermodynamic behavior. Am Mineral 87:648–657

Tribaudino M, Mantovani L, Bersani D, Lottici PP (2012) Raman spectroscopy of (Ca, Mg)MgS_i2_O6 clinopyroxenes. Am Mineral 97:1339–1347

Tribaudino M, Mantovani L, Mezzadri F, Calestani G, Bromiley G (2018) The structure of $P2_1/c$ ($Ca_{0.2}Co_{0.8}$)$CoSi_2O_6$ pyroxene and the $C2/c$ - $P2_1/c$ phase transition in natural and synthetic pyroxenes. Mineral Mag 82:211–228

Valenzano L, Torres FJ, Doll K, Pascale F, Zicovich-Wilson CM, Dovesi R (2006) Ab Initio study of the vibrational spectrum and related properties of crystalline compounds; the case of $CaCO_3$ calcite. Zeitsch Phys Chem 220:893–912

Wang A, Jolliff BL, Haskin LA, Kuebler KE, Viskupic KM (2001) Characterization and comparison of structural and compositional features of planetary quadrilateral pyroxenes by Raman spectroscopy. Am Mineral 86:790–806

Weinbruch S, Styrsa V, Muller WF (2003) Exsolution and coarsening in iron-free clinopyroxene during isothermal annealing. Geochim Cosmochim Acta 67:5071–5082

Wu Z, Cohen RE (2006) Generalized gradient approximation made more accurate for solids. Phys Rev B 73:235116